The Astrophysical Journal Supplement Series, 189:270–285, 2010 August doi:10.1088/0067-0049/189/2/270

THE MULTIWAVELENGTH SURVEY BY YALE–CHILE (MUSYC): DEEP MEDIUM-BAND OPTICAL IMAGING AND HIGH-QUALITY 32-BAND PHOTOMETRIC REDSHIFTS IN THE ECDF-S*

Carolin N. Cardamone[1,2], Pieter G. van Dokkum[1], C. Megan Urry[1,2], Yoshi Taniguchi[3], Eric Gawiser[4], Gabriel Brammer[1], Edward Taylor[5,6], Maaike Damen[5], Ezequiel Treister[7], Bethany E. Cobb[8], Nicholas Bond[4], Kevin Schawinski[2,13], Paulina Lira[9], Takashi Murayama[10], Tomoki Saito[11], and Kentaro Sumikawa[12]

[1] Department of Astronomy, Yale University, New Haven, CT 06511, USA; carolin.cardamone@astro.yale.edu
[2] Yale Center for Astronomy and Astrophysics, Yale University, P.O. Box 208121, New Haven, CT 06520, USA
[3] Research Center for Space and Cosmic Evolution, Ehime University, Bunkyo-cho 2-5, Matsuyama 790-8577, Japan
[4] Department of Physics & Astronomy, Rutgers University, Piscataway, NJ 08854-8019, USA
[5] Sterrewacht Leiden, Leiden University, NL-2300 RA Leiden, The Netherlands
[6] School of Physics, The University of Melbourne, Parkville 3010, Australia
[7] Institute for Astronomy, 2680 Woodlawn Drive, University of Hawaii, Honolulu, HI 96822, USA
[8] Department of Astronomy, University of California, Berkeley, CA 94720-3411, USA
[9] Departamento de Astronoma, Universidad de Chile, Casilla 36-D, Santiago, Chile
[10] Astronomical Institute, Graduate School of Science, Tohoku University, Aramaki, Aoba, Sendai 980-8578, Japan
[11] Institute for Physics and Mathematics of the Universe, The University of Tokyo, 5-1-5 Kashiwanoha, Kashiwa, Chiba 277-8583, Japan
[12] Graduate School of Science and Engineering, Ehime University, Bunkyo-cho, Matsuyama 790-8577, Japan
Received 2010 February 15; accepted 2010 June 8; published 2010 July 12

ABSTRACT

We present deep optical 18-medium-band photometry from the Subaru telescope over the $\sim 30' \times 30'$ Extended Chandra Deep Field-South, as part of the Multiwavelength Survey by Yale–Chile (MUSYC). This field has a wealth of ground- and space-based ancillary data, and contains the GOODS-South field and the Hubble Ultra Deep Field. We combine the Subaru imaging with existing *UBVRIzJHK* and *Spitzer* IRAC images to create a uniform catalog. Detecting sources in the MUSYC "*BVR*" image we find ∼40,000 galaxies with $R_{AB} < 25.3$, the median 5σ limit of the 18 medium bands. Photometric redshifts are determined using the EAzY code and compared to ∼2000 spectroscopic redshifts in this field. The medium-band filters provide very accurate redshifts for the (bright) subset of galaxies with spectroscopic redshifts, particularly at $0.1 < z < 1.2$ and at $z \gtrsim 3.5$. For $0.1 < z < 1.2$, we find a 1σ scatter in $\Delta z/(1+z)$ of 0.007, similar to results obtained with a similar filter set in the COSMOS field. As a demonstration of the data quality, we show that the red sequence and blue cloud can be cleanly identified in rest-frame color–magnitude diagrams at $0.1 < z < 1.2$. We find that ∼20% of the red sequence galaxies show evidence of dust emission at longer rest-frame wavelengths. The reduced images, photometric catalog, and photometric redshifts are provided through the public MUSYC Web site.

Key words: catalogs – cosmology: observations – galaxies: evolution – galaxies: formation – surveys

Online-only material: color figures

1. INTRODUCTION

Studies of distant galaxies and active galactic nuclei (AGNs) require redshift measurements to determine distances and associated look-back times. For optically bright objects, redshifts can be measured efficiently with multi-slit spectrographs on large telescopes (Davis et al. 2003; Le Fèvre et al. 2005). However, spectroscopic redshift measurements are very difficult for galaxies and AGNs that are at $z > 1$, obscured, or intrinsically faint. As a result, we had to rely almost exclusively on photometric redshifts determined from broadband photometry for galaxies with $I \gtrsim 23$ (see, e.g., Grazian et al. 2006; Wuyts et al. 2008, and many other studies).

The COMBO-17 survey (Wolf et al. 2004) pioneered the use of medium-bandwidth filters as a compromise between imaging and spectroscopy. These filters sample the spectral energy distributions (SEDs) of galaxies at a resolution of $R = 10$–20 and provide a redshift quality of 1%–2%, intermediate between spectroscopy and broadband imaging. This improvement enables measurements of rest-frame colors and the environment of galaxies, and improves the accuracy of determinations of the physical properties of galaxies. It also opens up the possibility of directly detecting strong emission lines, which is particularly relevant for the identification of AGN.

With the development of medium-band filter sets in the near-IR (van Dokkum et al. 2009) and on 8 m class telescopes (Ilbert et al. 2009), accurate redshifts are now becoming available for objects that are well beyond the limits of spectroscopy, and the full potential of this technique is being realized.

In this paper, we present deep 18-band optical medium-band photometry from the Subaru telescope in the $\sim 30' \times 30'$ "Extended" Chandra Deep Field-South (ECDF-S), as part of the Multiwavelength Survey by Yale–Chile (MUSYC; Gawiser et al. 2006b). The ECDF-S field has an extensive set of ancillary data (see Taylor et al. 2009), recently augmented by very deep *Spitzer* Infrared Array Camera (IRAC) data in the SIMPLE[14] survey (M. Damen et al. 2010, in preparation). Furthermore, the field contains the GOODS-South field and the Hubble Ultra Deep Field. Our medium-band survey is similar to that of Ilbert et al. (2009) in the larger COSMOS field, although we include 18 medium bands while there are only 12 available for the larger COSMOS field.

We discuss the observations in Section 2 and the details of data reduction in Section 3. We include ancillary data in our catalog

* Based (in part) on data collected at Subaru Telescope, which is operated by the National Astronomical Observatory of Japan.
[13] Einstein Fellow.
[14] http://www.astro.yale.edu/dokkum/SIMPLE/

Table 1
Medium-band Observations

Band (1)	FWHM (nm) (2)	Date Observed (3)	No. of Exposure (4)	Exposure time (s) (5)
IA427	21	2006 Jan 30	7	2100
IA445	20	2007 Jan 19	9	5400
IA464	22	2006 Jan 31	7	2940
IA484	23	2007 Jan 17	9	5400
IA505	26	2006 Jan 30	8	2400
IA527	24	2007 Jan 17	9	5400
IA550	28	2007 Jan 19	9	5400
IA574	27	2006 Jan 30	7	2100
IA598	30	2007 Jan 18	8	4800
IA624	30	2006 Dec 20	10	6000
IA651	33	2007 Jan 18	9	5400
IA679	34	2006 Dec 18	7	6300
IA709	32	2006 Jan 29	7	4200
IA738	33	2007 Jan 16	19	11400
IA767	37	2006 Dec 19	5	4200
IA797	35	2006 Dec 19	4	4800
IA827	34	2006 Jan 28	4	3600
IA856	34	2006 Dec 20	4	2400

from the MUSYC Survey, which is described in Section 4. The details of our photometry are discussed and the public catalog is presented in Section 5. We describe the photometric redshift determinations and evaluate the improvements provided by medium-band filters in Section 6. Finally in Section 7 we present the color–magnitude diagrams of the ECDF-S out to redshift 1.2 and investigate the occurrence of dusty galaxies on the red sequence. Throughout this paper we assume $H_0 = 71$ km s^{-1} Mpc^{-1}, $\Omega_m = 0.3$, and $\Omega_\Lambda = 0.7$.

2. OBSERVATIONS

We carried out a medium-band imaging campaign on the Subaru Telescope using the wide field-of-view camera Suprime-Cam (Miyazaki et al. 2002; Iye et al. 2004). Observations were collected in six runs over 2 years, in 2006 January, February, and December and 2007 January, March, and December; the observations are summarized in Table 1. We show the response curves of the medium-band filters used in this study in Figure 1. These filters were designed to maximize the accuracy of photometric redshifts by evenly sampling the wavelength range from 400 to 900 nm with an effective resolution of $\lambda/\Delta\lambda \sim 23$ (Taniguchi 2004).

Suprime-Cam consists of ten 2k $\times$ 4k CCD chips that cover a large field of view ($24' \times 27'$). A single raw exposure in filter IA651 is shown in Figure 2; each of the 10 individual chips show large gradients in background (from sensitivity variations and vignetting), as well as regions of bad pixels, and there are small gaps between the individual CCDs. Therefore, our observing strategy consisted of taking multiple Suprime-Cam exposures, slightly dithering the pointing to cover the small chip gaps. The median number of individual exposures for a given filter was nine, but the number of exposures and the exposure time were varied depending on conditions at the telescope and the available time each night. The long exposure on $IA738$ was designed to be used as a detection image for relevant science projects, but for our purposes here we prefer the significantly deeper MUSYC *BVR* image as a detection image. Table 1 lists (1) each filter, (2) the full width at half-maximum in nanometers, (3) its observation date, (4) the number of dithered exposures, (5) and the total exposure time in seconds.

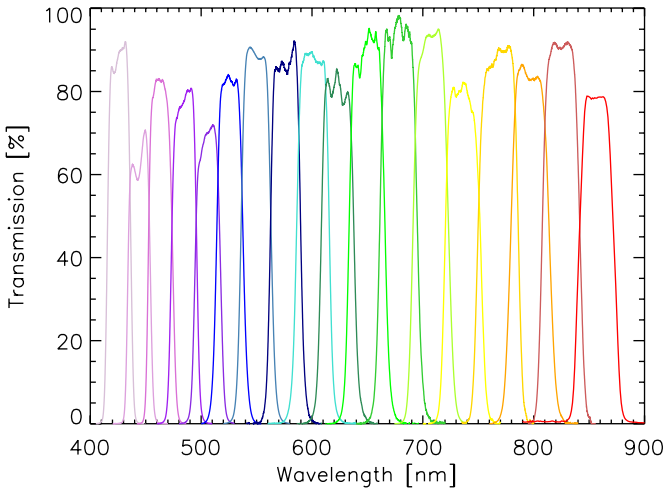

Figure 1. Subaru medium-band filter transmission curves, including atmospheric transmission, quantum efficiency, and the transmission of the optical elements of the telescope plus instrument. This filter set was designed to sample the spectrum evenly between 400 and 900 nm with an effective resolution of $\lambda/\Delta\lambda \sim 23$ in order to compute accurate photometric redshifts.

(A color version of this figure is available in the online journal.)

3. DATA REDUCTION

The data were reduced using a combination of standard IRAF[15] tasks: `sdfred`, a data reduction and analysis software package written for Suprime-Cam (Yagi et al. 2002; Ouchi et al. 2004), and custom tasks. Our reduction procedures follow those of Labbé et al. (2003) and Quadri et al. (2007), and are briefly described here.

3.1. Flat Fielding and Bias Subtraction

Dome flats are well exposed with high signal-to-noise ratios (S/Ns) and show the pixel-to-pixel variations on the CCD, while dark sky flats more accurately reproduce the variation in sensitivity to the night sky spectrum and the illumination pattern across the CCDs. Therefore, for each filter both dome flats and dark sky flats are constructed. We divide the high-S/N dome flats by the dark sky flats, effectively removing the differences between the CCD response to the dome lights and the light of the night sky, i.e., flattening the dome flats. To maintain the high S/N, we then smooth the resulting flats with the IRAF routine `boxcar`. The smoothing kernel for the `boxcar` routine was selected to be 10 pixels on a side because this minimizes the variance between adjacent smoothed areas ($\leqslant$0.1%); this effectively increases our S/N by an order of magnitude.

We also constructed master bias frames, combining ~10–20 bias frames collected each observing run with the IRAF routine `zerocombine`. One master bias frame per run was sufficient as the bias frames were stable from night to night.

After we construct the flat and bias frames, we apply them to the raw data frames. First, the two-dimensional master bias frames are subtracted from each raw data frame, and then the remaining overscan correction is subtracted using `sdfred`. Next, flat fielding is done by first dividing the raw science exposures by the dome flat and then dividing this by our

[15] IRAF is distributed by the National Optical Astronomy Observatory, which is operated by the Association of Universities for Research in Astronomy, Inc., under a cooperative agreement with the National Science Foundation.

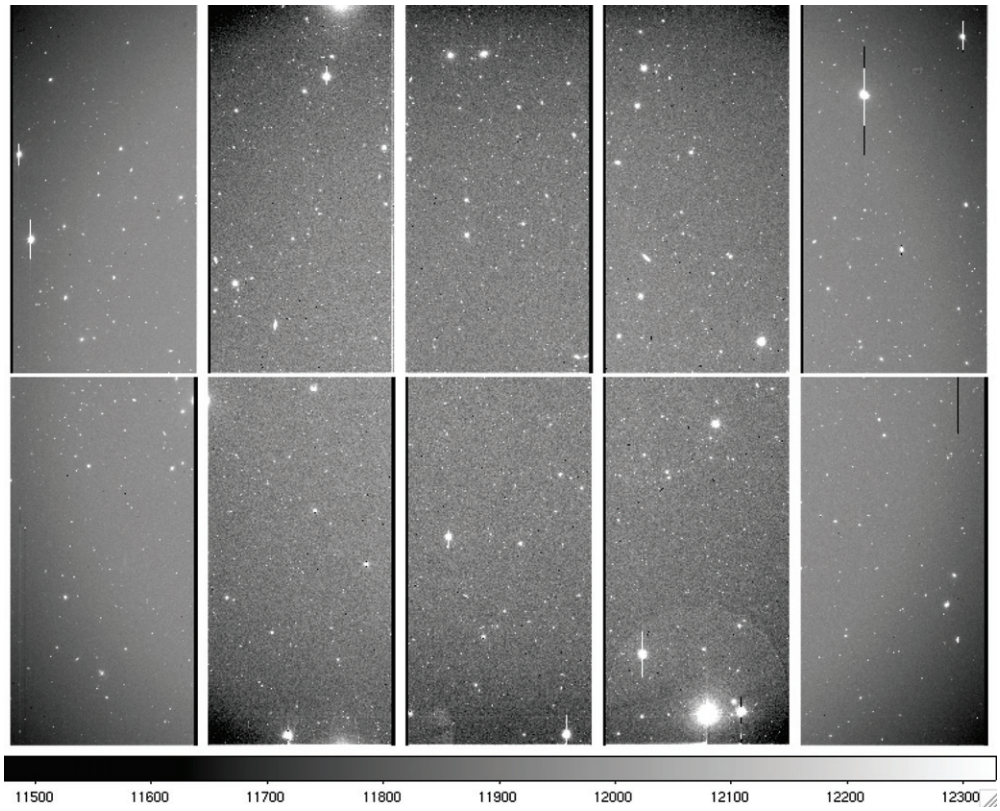

Figure 2. Example raw data frame from Suprime-Cam, for a 600 s exposure in Filter IA651 taken on 2007-1-18 (east is up, north is right). Each exposure is composed of 10 CCDs in a 5 × 2 array with small gaps between each chip. There are large gradients in the background illumination of each chip from sensitivity variations and vignetting. There are bad pixel columns and regions of low sensitivity near the chip edges, which must be accounted for in the data reduction.

smoothed sky flat as follows:

$$\frac{\text{rawframe} - \text{bias}}{\text{domeflat}} \times \left(\frac{\text{domeflat}}{\text{skyflat}}\right)_{\text{smoothed}}. \quad (1)$$

Even after careful flat fielding, small gradients in the sky background can remain that can affect photometry non-uniformly across the field. Using `SExtractor` (Bertin & Arnouts 1996), we measured and removed the sky gradient across the field using a large two-dimensional mesh (1000 pixels on a side). The large mesh was selected to avoid overestimating the sky near the edges of extended objects and near the location of faint objects not detected in individual exposures.

3.2. Image Combination

After flat fielding and bias subtraction, we are left with multiple individual exposures for each filter, each composed of 10 chips, ready to be combined. These chips must be aligned and then combined, preserving the flux in the stars and rejecting bad pixel artifacts.

Suprime-Cam provides a very large field of view, but with large geometric distortions caused by the optics. These distortions must be corrected for when combining individual dithered data frames into a final image. For a first-order coordinate correction, we use the standard task in `sdfrd`. Then we apply a secondary correction using the deep *BVR* combined image from the MUSYC Survey (Gawiser et al. 2006b) using the `IRAF` routine `mscimatch`.[16]

[16] The MSCRED package in IRAF was originally developed for mosaic reductions by NOAO. Information about the NOAO Mosaic Project can be found at http://www.noao.edu/kpno/mosaic/mosaic.html.

In our image combination, we maximize the S/N in the seeing disk of point sources by combining the individual CCD chips from each exposure using a weighted average. The weighted average is determined by the rms of the sky, the average FWHM, and the relative flux scale for each of the individual CCD exposures, following the procedure described in detail in Appendix A of Gawiser et al. (2006b), which was used in creating the broadband point-source-optimized images for the MUSYC Survey. This results in an optimal weight for each individual CCD chip as they are combined to make the final image. The weights are normalized to the first exposure central bottom chip.

Additionally, to improve our image quality, we use carefully constructed bad pixel maps when combining the final images. Bad pixel maps are first created from pixels marked by `sdfred`, including bad columns, isolated dead pixels, and the CCD chip edges. Then careful visual inspection is made of each exposure and all bad pixels found by eye, in addition to artifacts such as satellite trails, are included in the final bad pixel maps.

The final images are then created by averaging each of the individual weighted chips, rejecting the bad pixels, and using the `IRAF` routine `combine` with a percentile clipping algorithm. Experimentation showed that the percentile clipping algorithm provided optimal cosmic ray rejection. In Figure 3, we show final reduced images for $IA651$. On the left of Figure 3, we show the entire frame to show the flatness that we achieved across the image, while the right panel zooms in on the region displayed in the green box in the left panel. In the zoom-in, we see that many galaxies are clearly visible to the eye, the local background is relatively flat and no cosmic rays remain. We list details about each final combined image in Table 2. The

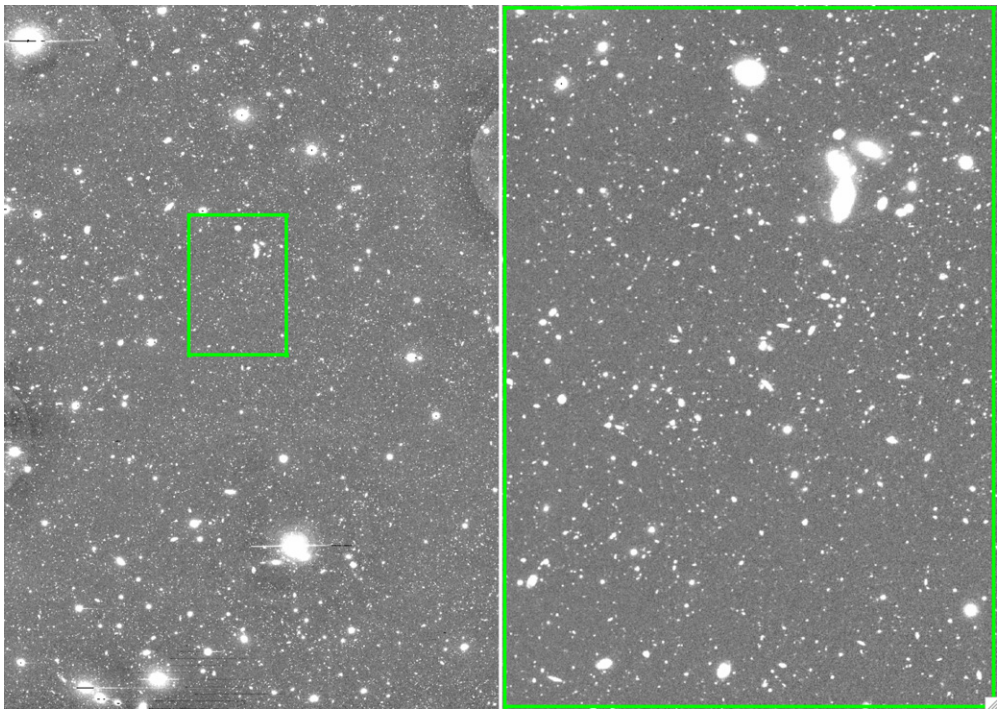

Figure 3. Left: full frame showing the final combined image in filter *IA*651, rotated 90° from the raw frame shown in Figure 2 (north is up, east is to the left). Note the uniformity across the field from careful attention to flat fielding and the dithering pattern of individual exposures. The S/N at the edge of the field is lower due to the smaller number of individual exposures combined at the edges with our dither pattern. A box indicates the region of the field displayed in the right panel, zooming in by a factor of 5. Right: detail of a final combined image in the filter *IA*651. Note the detailed morphology visible for nearby large galaxies.
(A color version of this figure is available in the online journal.)

Table 2
Medium-band Image Properties

Band (1)	FWHM (″) (2)	5σ depth (AB)[a] (3)	Zero Point (AB) (4)
IA427	1.01	25.01	25.10 ± 0.11
IA445	1.23	25.18	25.07 ± 0.08
IA464	1.79	24.38	25.30 ± 0.03
IA484	0.76	26.22	25.50 ± 0.05
IA505	0.94	25.29	25.34 ± 0.02
IA527	0.83	26.18	25.72 ± 0.03
IA550	1.13	25.45	25.88 ± 0.06
IA574	0.95	25.16	25.71 ± 0.02
IA598	0.63	26.05	26.02 ± 0.03
IA624	0.61	25.91	25.89 ± 0.05
IA651	0.60	26.14	26.15 ± 0.03
IA679	0.80	26.02	26.20 ± 0.03
IA709	1.60	24.52	26.02 ± 0.03
IA738	0.77	25.93	26.02 ± 0.02
IA767	0.70	24.92	26.04 ± 0.02
IA797	0.68	24.69	26.02 ± 0.02
IA827	1.69	23.60	25.92 ± 0.04
IA856	0.67	24.41	25.73 ± 0.01

Note. [a] Total magnitude.

FWHM, Column 2, is calculated using the `IRAF` routine `imexam` on several hundred stars.

3.3. Photometric Calibration

We now have a single final image for each filter, but these must be placed on a standard flux scale. To achieve this, each night at the telescope a handful of ESO spectro-photometric standard stars[17] were observed. These stars are used to calculate the zero point for each final image.

We calculate the magnitudes for these standard stars in our filter system (m_{ss}) by convolving the ESO standard star spectra with the effective transmission in each filter. We can then calculate the zero point for each filter, using the amount of flux observed in each star ($\mathrm{flux_{obs}}$) in the standard star images. The zero point for the final image in each filter is given by

$$m_{zp} = m_{ss} - 2.5 \times \log \mathrm{flux_{obs}} - \mathrm{airmass} \times k_\nu. \quad (2)$$

Here k_ν, the airmass coefficient, stands for the extinction in magnitudes per airmass and is necessary because each standard star observation was made at a different airmass from the science images. To determine k_ν, we first obtained the Extinction Curve for Mauna Kea from the Canada–France–Hawaii Telescope (CFHT) observers' manual[18] and compared this to an extinction curve derived on Mauna Kea in the *B* and *V* bands published by Krisciunas et al. (1987). Additionally, on nights when a single standard star was observed at multiple airmasses, we directly calculated extinction curves. All k_ν measurements were consistent with each other. Therefore when calculating the zero points for each filter, we used our own measured values for the six filters for which they were available (*IA*427, *IA*484, *IA*527, *IA*624, *IA*738, and *IA*856), two additional values from Krisciunas et al. (1987), the *B* band for *IA*445, and the *V* band for *IA*550; we interpolated values for the remaining 10 filters according to the curve published by the CFHT. The fluxes are normalized such that they are fluxes

[17] http://www.eso.org/sci/observing/tools/standards/spectra/
[18] http://www.cfht.hawaii.edu/Instruments/ObservatoryManual/CFHT_Observatory_Manual_TOC.html

per second, to account for the different exposure times of the standard stars and the final image exposures. The airmass assigned to the final combined image is that of the first exposure, which is used to normalize the flux in the image combination (Section 3.2). The zero points for each filter are listed in Table 2, Column 4.

3.4. Noise Properties

The noise properties of each final image must be understood in order to calculate the nominal depth of each final combined image, as well as accurate photometric errors. SExtractor assumes Poisson sky noise and thus can underestimate the total errors in the photometry, which include contributions from electron readout noise, sky noise, imperfect background subtraction, and pixel-to-pixel correlations that can be introduced during the reduction process. To accurately account for all of these effects, we sum the counts in a large number of apertures randomly placed throughout the image, and add these error estimates in quadrature with the output error from SExtractor (Labbé et al. 2003; Gawiser et al. 2006b; Quadri et al. 2007). The apertures are placed in locations to avoid objects (using SExtractor's segmentation map) and have an identical size to the photometry apertures we later use in each band (see Section 5). The roughly Gaussian distribution of flux in these apertures describes the noise in the background on the image, and the sigma width of this Gaussian measures the uncertainty in the background noise (i.e., the depth) of the imaging. These depths are based on flux measurements within the aperture size used for photometry. Integrating over the point spread function (PSF), an offset of -0.6 mag is necessary to correct these magnitudes from aperture values to total values (see Section 5.2). We report 5σ depths with this correction in Table 2, Column 3. We note an independent analysis of these same data gives slightly different zero points and depths, due to small differences in methodology. The zero points are consistent to $\sim$0.1 mag for all filters.

3.5. Final Images

We created final combined images for each filter (Figure 3), which are available from the MUSYC Web site.[19] We list each image and its properties in Table 2: Column 1 lists the central wavelength of the filter in nanometers, Column 2 lists the seeing, as measured using the average FWHM of a sample of several hundred stars in the actual image, Column 3 lists the 5σ depth in AB magnitudes, and Column 4 lists the zero-point value for the image.

4. ANCILLARY DATA

4.1. MUSYC Survey: Existing Optical and Near-infrared Data

The ECDF-S has been targeted by a host of optical and infrared surveys (Arnouts et al. 2001; Moy et al. 2003; Wolf et al. 2004; Gawiser et al. 2006b; Hildebrandt et al. 2006; M. Damen et al. 2010, in preparation). We obtain reduced optical and near-infrared imaging from Taylor et al. (2009), where the observations, reductions, and characteristics of these data are described in detail. To summarize briefly, the $UU_{38}BVRI$ imaging originates from the ESO archive and were combined from multiple projects using the Wide Field Imager (WFI) on the ESO MPG 2.2 m telescope. These data were collected and calibrated as part of the Garching-Bonn Deep Survey (GaBoDS; Hildebrandt et al. 2006). The z-band data, collected as part of the MUSYC Survey, are from the Mosaic-II camera on the Cerro Tololo Inter-American Observatory (CTIO) 4 m Blanco telescope (Muller et al. 1998) and are described further by Gawiser et al. (2006b) and Taylor et al. (2009). The H-band data, taken with SofI on the ESO NTT 3.6 m telescope (Moy et al. 2003), covers 80% of the field (Taylor et al. 2009). The JK imaging was obtained using the ISPI camera on the CTIO Blanco 4 m telescope (Taylor et al. 2009). The images along with the size of the FWHM, 5σ depth, zero point, and survey in which they were observed, are listed in Table 3. The FWHM and 5σ depth are measured in the same way we determined these values for the Subaru data (Section 3.4 3.2) and are listed in Columns 2 and 3 of Table 3. We adopt the calibration and zero points published in Taylor et al. (2009), shown here in Column 4.

Table 3
Other Optical and Infrared Data

Band (1)	FWHM ($''$) (2)	5σ Depth (AB)[a] (3)	Zero Point (AB) (4)	Survey (5)
BVR	0.83	26.82	23.58	MUSYC[b]
U38	0.98	25.33	21.96	GaBoDS[c]
U	1.05	25.86	22.74	GaBoDS[c]
B	1.01	26.45	24.38	GaBoDS[c]
V	0.94	26.27	24.10	GaBoDS[c]
R	0.83	26.37	24.66	GaBoDS[c]
I	0.96	24.30	23.66	GaBoDS[c]
z	1.07	23.69	24.47	MUSYC[a,d]
J	1.48	22.44	23.53	MUSYC[a,d]
H	1.49	22.46	24.15	ESO[e]
K	0.94	21.98	24.40	MUSYC[a,d]
3.6 μm	2.08	23.89	22.42	SIMPLE[f]
4.5 μm	2.01	23.75	22.19	SIMPLE[f]
5.8 μm	2.21	22.42	20.60	SIMPLE[f]
8.0 μm	2.28	22.50	21.78	SIMPLE[f]

Notes.
[a] Total magnitude.
[b] Gawiser et al. (2006a).
[c] Hildebrandt et al. (2006).
[d] Taylor et al. (2009).
[e] Moy et al. (2003).
[f] M. Damen et al. 2010, in preparation.

4.2. SIMPLE Survey

Considerable *Spitzer* time has been invested in the ECDF-S with both IRAC (Fazio et al. 2004) and the Multi-Band Imaging Photometer for *Spitzer* (MIPS; Rieke et al. 2004). The *Spitzer* IRAC/MUSYC Public Legacy in the ECDF-S (SIMPLE; M. Damen et al. 2010, in preparation) project obtained very deep IRAC imaging across the full ECDF-S. The IRAC data cover 3–8 μm, to $\sim$24th magnitude AB at 3.6 μm. The astrometry was calibrated using the MUSYC *BVR* detection image, the same image we used in the Subaru medium-band reductions (Section 3.2); the resulting positional accuracy for individual sources is $\lesssim$0.3 arcsec (1σ; M. Damen et al. 2010, in preparation). We include the IRAC data from the SIMPLE Survey in Table 3. The values for FWHM (Column 2) and 5σ depth (Column 4) are measured in the same manner as for the ground-based imaging (Section 3.4, 3.2). The zero-point values (Column 4) come from M. Damen et al. (2010, in preparation).

[19] http://physics.rutgers.edu/~gawiser/MUSYC

4.3. Astrometric Calibration

In order to perform multi-band photometry, each image is transformed to the image plane and pixel scale (0.″267) of the stacked *BVR* image used for detection (Gawiser et al. 2006b). The rms astrometric errors, compared to an astrometric catalog of the ECDF-S, are estimated to be less than 0.″2 across the entire field (Gawiser et al. 2006b). Using IRAF tasks `geomap` and `geotran` all images were resampled to the coordinate system of the *BVR* image (both in x–y pixel coordinates and in right ascension and declination) with a north-up tangent plane projection.

5. PHOTOMETRY

In order to create accurate multiwavelength SEDs, a constant fraction of light needs to be collected for each object across every band. If the varying PSFs of each band are not taken into account, similar apertures will collect different fractions of an object's total light. The data in our survey come from a variety of telescopes, with large variations in seeing (Tables 2 and 3, Column 2). Experiments with the broadband images showed that failure to correct for this effect would bias the $U-V$ colors of sources by up to ∼20%. Therefore, close attention was paid to obtaining accurate colors. In this section, we describe the methodology used to measure accurate colors (Section 5.1), the selection of the apertures to be used for the photometry (Section 5.2), the detection of objects on the images (Section 5.3), and the completeness of our detection as a function of object magnitude (Section 5.4).

5.1. PSF Matching

We have a total of 10 ground-based broadband images (U, $U38$, B, V, R, I, z, J, H, K), 4 IRAC images (3.6 μm, 4.5 μm, 5.8 μm, 8.0 μm), and 18 medium-band images ($IA427$, $IA445$, $IA464$, $IA484$, $IA505$, $IA527$, $IA550$, $IA574$, $IA598$, $IA624$, $IA651$, $IA679$, $IA709$, $IA738$, $IA767$, $IA797$, $IA856$). The seeing in these images ranges from ∼0.″5 to over 2″ (Tables 2 and 3). In this section, we describe our technique for smoothing multiple images to the same PSF to correctly measure color fluxes.

One technique commonly used to achieve uniform photometry across images in multiple filters relies on smoothing all images to the PSF size of the image with the worst seeing (e.g., Labbé et al. 2003; Capak et al. 2007; Taylor et al. 2009). Then large apertures are used for photometry, collecting flux within a uniform physical area across all images for each galaxy. However, degrading all images to the largest PSF size significantly decreases the S/N in each filter where the image is smoothed. Given the large range in PSF size across our data, if we degraded all images to the worst seeing we would sacrifice the excellent image quality found in the majority of our observations.

Therefore, we apply a two-fold approach. First, for the 12 images with narrow PSFs (Tables 2 and 3), we smooth them to the PSF of the *BVR* ∼ 0.″8 image. For these images, all fluxes are measured using a single aperture, which in this case provides accurate PSF-matched photometry. Then, for the images with PSFs larger than that of the *BVR* image (Tables 2 and 3), we degrade a copy of the *BVR* image to match each of the larger PSF sizes. We can then measure a color, e.g., $f_{(K)} - f_{(BVR,\mathrm{smoothed})}$, and scale this to the aperture flux measured in the *BVR* 0.″79 image, $f_{(BVR)}$. In other words, the PSF-matched K-band flux is

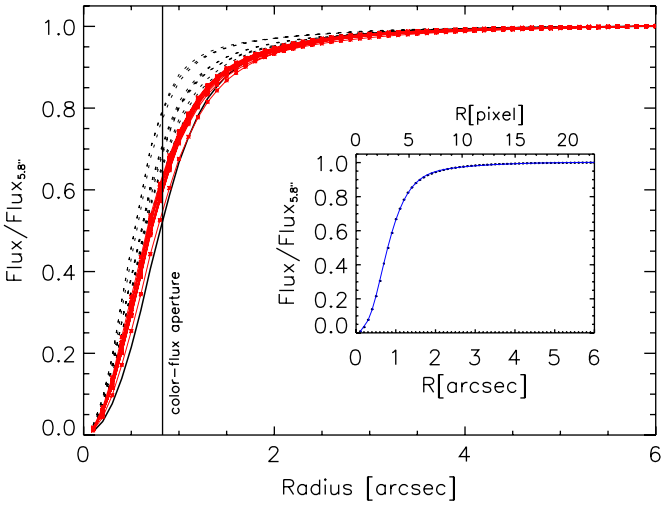

Figure 4. Stellar curve of growth for the 12 bands with PSFs smaller than the *BVR* PSF (black dashed lines), measured using 20 isolated stars. Red solid lines show the smoothed PSF after convolution with the appropriate kernel to match the *BVR* PSF; also indicated is the aperture used for the PSF-matched flux. Inset: *BVR* stellar curve of growth and fifth-order polynomial fit. We use this curve to measure the fraction of light missed in an aperture of a given size, and thus the correction to total flux (Section 5.3).

(A color version of this figure is available in the online journal.)

measured by

$$f_{(K,\mathrm{psf\ matched})} = f_{(K)} \times \frac{f_{(BVR)}}{f_{(BVR,\mathrm{smoothed})}}. \quad (3)$$

Here $f_{(BVR)}$ is the flux measured in the *BVR* image with its native 0.″8 seeing, and $f_{(BVR,\mathrm{smoothed})}$ is the flux measured in the copy of the *BVR* image, smoothed to have the same seeing as the K-band image. Therefore, $f_{(K,\mathrm{psfmatched})}$ provides accurate colors when compared to the fluxes measured from the 12 images with narrow PSFs. We note that the aperture radius in which the flux is measured is selected to be the FWHM (see Section 5.2), so to measure the flux in the K-band image ($f_{(K)}$) and the smoothed *BVR* image ($f_{(BVR,\mathrm{smoothed})}$), we use an aperture radius equal to the FWHM of the K-band image. We note that in Equation (3), K represents any of the filters whose final images have PSF sizes larger than the *BVR* image (U, $U38$, B, V, I, z, J, H, K, $IA427$,$IA445$, $IA464$, $IA505$, $IA550$, $IA574$, $IA709$, and 3.6, 4.5, 5.8, 8.0 μm). The final catalog contains these PSF-matched fluxes for each of the 32 bands.

Here we describe our technique for smoothing two images to an identical PSF. We first attempted to smooth the images with a Gaussian convolution kernel, but found that the residual PSF variations were large due to the non-Gaussian PSF shape for stars in the images. Instead, we decided to build a separate PSF for each filter directly from the images themselves. To do this, we selected ∼20 isolated stars in each band that were well exposed but not saturated. The selected stars were registered, normalized to their peak flux, and then averaged to create a single model PSF for each band. We used the Lucy–Richardson algorithm (IRAF's `lucy`) to construct a kernel to convolve with each image. In Figure 4, we show the stellar curve of growth for the 12 images with PSFs smaller than the *BVR* image (dotted lines). The corresponding new curves of growth for the 12 smoothed images (red lines), where we have convolved the original image with our Lucy–Richardson kernel to match the *BVR* image PSF, show a consistent stellar profile. The ratio of the flux enclosed within our photometry aperture to total

flux (measured within 6 FWHM) is stable to nearly ∼1%. This accuracy is also achieved in the smoothed copy of the *BVR* image for each filter with poor seeing.

5.2. Aperture Selection

In order to optimize the S/N for the photometry, the flux in each object is measured in the central high surface brightness regions of the objects and then later corrected to a total flux measurement. For a Gaussian PSF and uncorrelated noise, the aperture diameter that maximizes the S/N is 1.35 times the seeing FWHM (Gawiser et al. 2006b). We use an aperture radius equal to the seeing FWHM, which encloses ∼50% of the flux (Figure 4) and provides nearly optimal S/N for point-source photometry (Gawiser et al. 2006b).

We note that an aperture defined to ensure high S/N can result in fluxes that measure only the central region of galaxies, particularly for large galaxies at low redshifts. For example, at $z = 0.3$, a 0.″8 aperture is ∼4 kpc. Therefore, for a Milky Way size galaxy at redshift 0.3, our aperture would measure only the central bulge stars. Hence, any color gradients in the outer regions of the galaxy would not influence these aperture fluxes. Therefore, it is important to note that in our catalog, the fluxes describe only the central regions of the galaxies at lower redshift. We also emphasize the importance of measuring the same central fraction of each galaxy in the apertures (Section 5.1).

When measuring the noise in the image (Section 3.4), we used an aperture size equal to the seeing FWHM and converted these to total magnitudes assuming a stellar profile (Figure 4). Therefore, our 5σ depths are computed for point sources, a magnitude offset of −0.6 from the aperture depth derived from the images.

5.3. Source Detection

For object detection, we run SExtractor version 2.4.4 (Bertin & Arnouts 1996) in dual-image mode using the original *BVR* image for detection. In the 20 filters where a copy of the *BVR* image was smoothed to the image's larger PSF, SExtractor was run twice: first on the filter's image and then again on the smoothed *BVR* image (Section 5.1). SExtractor directly gives us aperture fluxes (with a radius of 2 × FWHM) for the images of the 12 filters with small PSFs. For the 20 filters with images with larger PSFs, we compute aperture fluxes from Equation (3).

To correct our aperture fluxes to total fluxes for each source, we compute a total-flux correction factor for each object. SExtractor's AUTO flux uses a flexible Kron-like (Kron 1980) elliptical aperture to compute the flux. The flux in this aperture accounts for the size of the source and the source shape, and measures approximately 94% of the total flux (Bertin & Arnouts 1996). We use SExtractor to obtain AUTO fluxes for each object from the *BVR* image. Then we correct this AUTO flux to a total flux using the stellar curve of growth from the *BVR* image (Figure 4 inset, points). We fit this growth curve with a fifth-order polynomial (Figure 4 inset, solid blue line) and compute the fraction of light enclosed for each object at the Kron radius (lightfrac). The total flux correction factor to be applied to the AUTO flux is then the inverse of the fraction of light enclosed at the AUTO flux radius for each source (totcor = 1/lightfrac). To correct our aperture fluxes in any given filter to total flux in that filter we scale the aperture flux using the ratio of the *BVR* AUTO flux to the *BVR* aperture flux for that source and then multiply it by the flux correction factor (totcor):

$$f_{K,\mathrm{tot}} = f_{K,\mathrm{aperture}} \times \frac{f_{BVR,\mathrm{AUTO}}}{f_{BVR,\mathrm{aperture}}} \times \mathrm{totcor}, \quad (4)$$

where K can be replaced here by any filter in our catalog. We note that for extended objects this is a minimum correction to a total magnitude (Taylor et al. 2009).

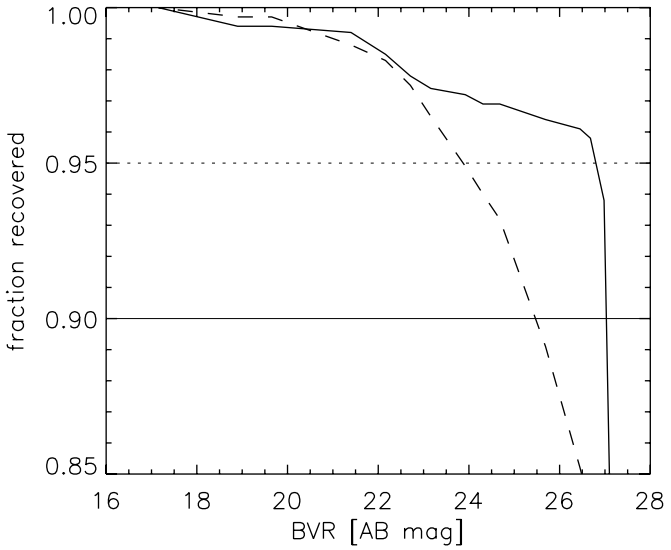

Figure 5. Fraction of simulated stars detected by SExtractor. For stars placed to avoid bright stars and the locations of other objects on the image (solid line), the 90%/95% completeness level is nearly 27 AB magnitudes. Stars placed randomly (dashed line) yield lower completeness because they suffer from source confusion. The 90% (95%) completeness for these simulated stars is ∼25.5 (24) AB magnitudes.

5.4. Completeness

Although we measure the nominal depth of our images using the background noise (Section 3.4) in empty apertures across the field, the actual completeness of our catalog is a strong function of source magnitude. For each filter in the catalog, the 5σ depth is listed in Tables 2 and 3; for the *BVR* detection image, this depth is 26.8 in AB magnitudes.

To empirically measure our overall effectiveness in detecting objects as a function of magnitude, we construct a stellar PSF, normalize it to various magnitudes, place it into the *BVR* detection image, and determine if SExtractor recovers the inserted star. The stellar image we use is that constructed from 20 well-exposed stars in Section 5.1 to measure the *BVR* image PSF. A thousand random locations are selected, at locations at least 10 pixels (∼3 FWHM) away from detected objects and avoiding regions of the field that are washed out by bright stars. Near larger objects (e.g., galaxies), distances to these random sources were increased to be greater than twice the Kron radius. We create multiple images, each with 1000 stars of varying magnitude and then run SExtractor on each of these new images. Figure 5 shows the percentage of these stars recovered as a function of simulated magnitude (solid line). The 95% completeness level is nearly 27 mag, and it falls quickly below that magnitude. This agrees well with the number determined from placing empty apertures around the field. However, in both cases we ignore the extent of detected objects on the field. Because real galaxies do overlap each other along the line of sight, we repeat this exercise, no longer restricting the random positions to avoid detected objects of this field (although we

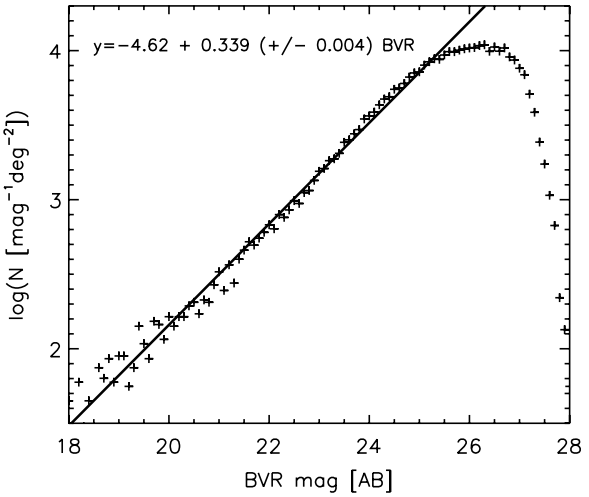

Figure 6. Number counts in the *BVR* band. The number of sources increases steadily to *BVR* ∼ 25.5 mag, our 90% completeness level. Our differential number count measurement 0.339 ± 0.004 is consistent with the value 0.34 ± 0.01 measured by Gawiser et al. (2006b).

still avoid the very bright stars which wash out large areas on the field). The recovery rate of these sources falls much faster at faint magnitudes, due to missing the inserted stars near brighter stars and galaxies (Figure 5, dashed line). Still, at a magnitude of ∼25.5 we are 90% complete in our detections.

Figure 6 shows our *BVR* band number counts for the *BVR*-detected catalog. The number counts increase steadily until *BVR* ∼ 25.5 mag [AB], where we are still 90% complete. Differential number counts can measure the geometry of space and the evolution of structure in the universe. Our fit to the differential number counts per magnitude per square degree is 0.339 ± 0.004, consistent with the 0.34 ± 0.01 measured by Gawiser et al. (2006b).

5.5. Galactic Extinction

The ECDF-S is at high Galactic latitude and therefore has a very low Galactic extinction. For the location of the ECDF-S, R.A. = 3^h32^m and decl. = $-27°48'$, we calculate a value of $E(B-V) = 0.0088$ from the 100 μm maps of Schlegel et al. (1998).[20] We calculate the expected Galactic extinction in each band, assuming $R = 3.1$ and using the Galactic Extinction Curve of Cardelli et al. (1989) with updates in the optical region from O'Donnell (1994). These values are listed in Table 6, Column 1. The Galactic extinction corrections are not included in the catalog, but are applied before photometric redshifts are computed (Section 6).

5.6. Catalog

We present our catalog format in Table 4, available online in full format.[21] The photometry is measured in units of flux (μJy) and is not corrected for Galactic extinction. For the *BVR* combined image, the `AUTO` flux as well as the `APERTURE` flux is included. The fluxes are aperture fluxes and can be corrected to total fluxes using the total flux correction and the AUTO flux (Equation (4)). The geometrical parameters are output from SExtractor including the Kron radius, `A_IMAGE`, `B_IMAGE`,`THETA_IMAGE`, and `CLASS_STAR`. The table is presented both as a text file and as a FITS file. In the FITS version of the catalog, SExtractor detection flags (Bertin & Arnouts 1996) for each filter are included.

6. REDSHIFTS

The Subaru imaging allows us to obtain accurate ($\Delta z/(1+z) \sim 0.01$) photometric redshifts for the sources in our catalog. In this section, we describe our method for computing photometric redshifts and evaluate their accuracy as determined by a subset of sources with spectroscopic redshifts.

6.1. EAzY

In order to obtain highly accurate photometric redshifts, we used EAzY, a program optimized to provide high-quality redshifts over $0 \leqslant z \leqslant 4$, where complete spectroscopic calibration samples are not available (Brammer et al. 2008). EAzY is a full-featured redshift fitting code, allowing for the use of priors in computing photometric redshifts (e.g., BPZ; Benítez 1999). It includes a user-friendly interface based on HYPERZ (Bolzonella et al. 2000) and a carefully selected template set, designed to optimize photometric redshifts for optical-NIR surveys (Brammer et al. 2008). The template set and the magnitude priors are based on semi-analytical models that are complete to very faint magnitudes, rather than highly biased spectroscopic samples, and so are particularly useful for samples of objects such as dust obscured galaxies that are faint in the optical (e.g., Treister et al. 2009a). When running EAzY, we allow for a linear combination of all templates and include a broad-line AGN template only when fitting sources detected in X-rays (Cardamone et al. 2008). The AGN template is based on the Sloan Digital Sky Survey (SDSS) QSO template from Vanden Berk et al. (2001), which we have extended toward the red using the mean QSO SED from Richards et al. (2006). Following Ilbert et al. (2009), EAzY now includes strong narrow emission lines in its galaxy templates by estimating an [O II] emission line flux from the UV luminosity of the scaled template and adopting fixed line ratios for [O III/O II], [Hβ/O II], and [Hα/O II] as defined by Kennicutt (1998). Further, EAzY introduces a template error function to account for wavelength-dependent template mismatch.

EAzY provides multiple estimates of the photometric redshift, including z_peak, which we adopt in this work as the photometric redshift estimate. Because z_peak is marginalized over the full probability distribution, it can differ from the best estimate from a straight χ^2 minimization when there are two widely separated peaks in the redshift probability function by selecting the peak with the largest integrated probability. Additionally, it includes an estimate of the quality of each photometric redshift (Q_z) which combines the χ^2 of the template fit, the width of the 68% confidence interval, and the BPZ odds parameter (Benítez 1999) in such a way that Q_z increases as any of those parameters deteriorates (Brammer et al. 2008). We recommend adopting a cut in Q_z, when using the photometric redshifts for science (see Brammer et al. 2008 and Section 6.5), and in this work adopt the conservative requirement of $Q_z \leqslant 1$ for all photometric redshifts used.

When using EAzY to compute our photometric redshifts, we include the 18 medium bands and the optical and near-infrared ground-based coverage in addition to the IRAC data. Example SEDs are shown in Figure 7. The FWHM of the broadband filters is indicated by a red line. We compute photometric redshifts for over 99% of sources in our *BVR*-detected catalog using the default EAzY output, and adopting the default template error

[20] http://www.astro.princeton.edu/∼schlegel/dust/data/data.html
[21] http://physics.rutgers.edu/∼gawiser/MUSYC

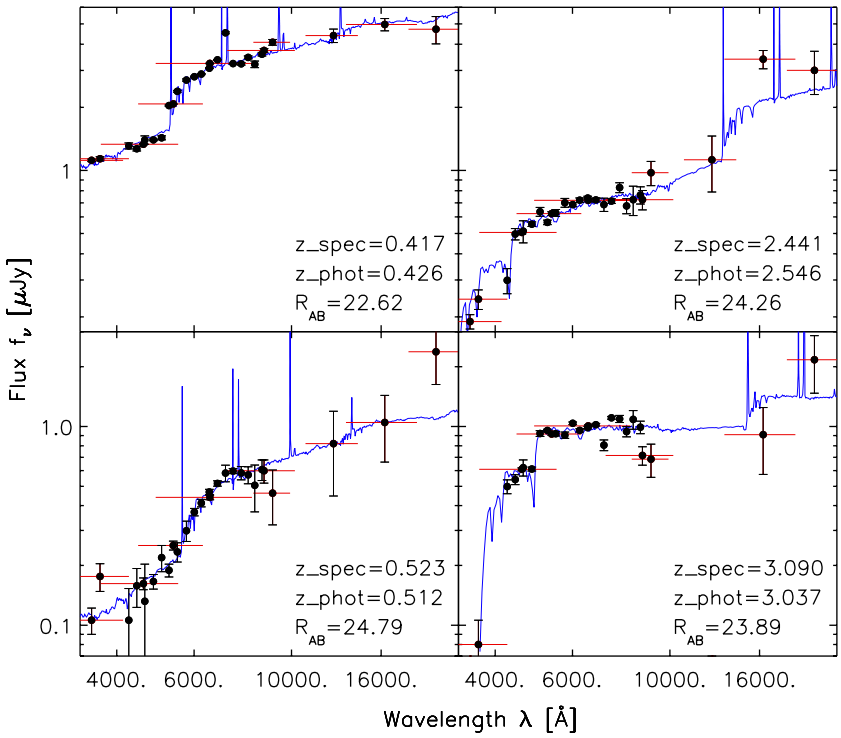

Figure 7. Example SEDs with EAzY spectral fits overlaid. In black are the data points with 1σ errors. The blue line shows the linear combination of template SEDs that best fit the data. In the left-hand column, we illustrate two low-redshift examples where the Balmer break is fit by the medium-band filters. In the right-hand column, we illustrate two high-redshift examples showing a break due to Lyα absorption. We highlight fits to faint sources, $R \sim 24$ in three of the four sources shown. Emission lines do influence the photometry.

(A color version of this figure is available in the online journal.)

Table 4
Summary of Photometric Catalog Contents

Column No.	Column Title	Description
1	num	Sequential Object Identifier, beginning from 0
2, 3	R.A., decl.	Right ascension and declination (J2000; decimal degrees)
4	CLASS_STAR	SExtractor parameter measuring stellarity of object
5	Kron radius	SExtractor parameter measuring source size in a flexible aperture (pixels)
6, 7	A_IMAGE,B_IMAGE	SExtractor parameter measuring major and minor axes of image profile (pixels)
8	THETA_IMAGE	SExtractor parameter measuring position angle measured counterclockwise from north (degrees)
9	totcor	Aperture correction to convert AUTO flux to total (μJy)
10, 11	f_auto_*BVR*,e_auto_*BVR*	SExtractor AUTO flux and error (μJy)
12–76	f_X,e_X	Aperture flux and error in each filter (μJy), including that measured for the *BVR* image
77	flag_X	*BVR* SExtractor detection flag[a]

Note. [a] In the FITS version of the table, SExtractor detection flags are included for all filters.

function and *R*-band photometric prior. For the less than 1% of *BVR*-detected sources that lie on the imaging area in fewer than five filters, we do not compute photometric redshifts.

6.2. Spectroscopic Redshifts

We collect all available spectroscopic redshifts for sources in our catalog from the literature in order to quantify our photometric redshift accuracy. The quality of these redshifts varies widely, from sources with multiple spectral line measurements to sources showing only hints of a single spectral line. Matching these spectroscopic redshifts to our catalog, there are almost ∼4000 unique objects with redshifts, ∼1000 of which have multiple published spectroscopic redshifts. For sources with multiple redshift determinations we select those with a higher quality flag, favoring redshift measurements with published quality flags over those without. In Table 5, we list all references from which unique spectroscopic redshifts were obtained, including the number of spectroscopic redshifts used from the data set, the source paper, the quality flags we used in determining the accuracy of our photometric redshifts, and the median *R*-band magnitude (Section 6.5). When evaluating the accuracy of the photometric redshifts, we restrict the quality of the spectroscopic redshifts used in the comparison. If we include spectroscopic redshifts with lower quality flags, it lowers the determined accuracy by factors of 2 or 3, independent of redshift or magnitude, and it increases the fraction of outliers. Each of the redshift catalogs adopted a different selection technique for the sources for which they obtained spectra: Balestra et al. (2010) selected galaxies at $1.8 < z < 3.5$ for the VIMOS

Table 5
Spectroscopy

No. of Sources (1)	References (2)	Quality Flags (3)	Median (R_{AB}) (4)
1239	Balestra et al. 2010	A	23
573	Vanzella et al. 2008	A,B	24
223	Le Fèvre et al. 2004	4,3	23
224	Cimatti et al. 2002	1,0	23
211	P. Lira et al. 2010, in prep.	3,2	22
52	Szokoly et al. 2004	3,2,1	23
9	Kriek et al. 2008	n/a	24
7	Treister et al. 2009b	1	23
5	Strolger et al. 2004	n/a	25
3	Cristiani et al. 2000	n/a	24.5
3	van der Wel et al. 2004	n/a	26
2	Croom et al. 2001	n/a	22

Low Resolution Blue grism and galaxies at $z < 1$, in addition to Lyman break Galaxies at $z > 3.5$ in the Medium Resolution (MR) orange grism; Vanzella et al. (2008) selected galaxies using color criteria and photometric redshifts at $0.5 < z < 2$ and $3.5 < z < 6.3$ for VLT/FORS2 observations; Le Fèvre et al. (2004) selected galaxies using a magnitude selection of $I_{AB} < 24$; Cimatti et al. (2002) selected galaxies using a magnitude selection of $K_s < 20$; P. Lira et al. (2010, in preparation) selected galaxies using a variety of criteria including sources with X-ray counterparts, Lyα emitters, and Lyman break galaxies at $2.7 < z < 3.6$; Szokoly et al. (2004) selected galaxies with X-ray counterparts; Kriek et al. (2008) selected K-bright galaxies at $z \sim 2.3$ using the BzK and DRG color selection (Daddi et al. 2004; Franx et al. 2003); Treister et al. (2009b) selected galaxies with X-ray counterparts; Strolger et al. (2004) selected high-redshift galaxies in a Supernova search; Cristiani et al. (2000) selected galaxies using the VLT UV-Visual Echelle Spectrograph to detect Lyα; van der Wel et al. (2004) selected galaxies at $z \sim 1$ from the COMBO-17 catalog with a compact and regular shape; and Croom et al. (2001) selected compact objects with $J-K$ colors redder than the stellar sequence. We note that many of these spectroscopic data sets have a larger number of total published redshifts; we include here only those that we have adopted as unique redshifts in our spectroscopic redshift catalog. Additionally, other references contain spectroscopic redshifts in the ECDF-S, but they are not mentioned here unless we adopt at least one spectroscopic redshift into our unique listing.

6.3. Zero-point Adjustments

To perform SED fitting, we require highly accurate colors across the optical and near-infrared spectrum. Photometric zero points (Tables 2 and 3, Column 4) were determined individually in each band through standard star measurements. However, small offsets of a few percent in adjacent bands can introduce significant color offsets. This is a particular concern when a catalog, like ours, includes photometry from a variety of instruments taken over a period of many years. If we assume that a priori we know the spectral shapes of the galaxies and that they can be well fit by our synthetic SED templates, than any systematic offsets of observed fluxes in a given filter are due to a photometric zero-point error in that filter. Because our sources cover a wide range of redshifts, each filter samples a different region in every rest-frame galaxy SED and therefore any systematic photometric offsets in this filter are due to zero-point offsets rather than a template error at a single wavelength.

Table 6
Photometric Zero-point Offsets from SED Fitting

Band (1)	Galactic Extinction (2)	ZP Correction (3)
U38	0.041	−0.184
U	0.043	−0.245
B	0.034	0.053
V	0.028	0.075
R	0.022	0.075
I	0.014	0.032
z	0.013	0.156
J	0.008	−0.023
H	0.005	−0.011
K	0.003	0.255
IA427	0.037	0.285
IA445	0.036	0.124
IA464	0.034	−0.057
IA484	0.032	0.075
IA505	0.030	0.146
IA527	0.029	0.010
IA550	0.027	0.126
IA574	0.026	0.054
IA598	0.024	0.064
IA624	0.023	0.116
IA651	0.022	0.032
IA679	0.021	−0.035
IA709	0.020	−0.001
IA738	0.019	0.054
IA767	0.018	0.086
IA797	0.017	0.075
IA827	0.016	−0.106
IA856	0.014	0.106

To cross-calibrate our photometry, we take the best-fit EAzY SED for each galaxy and measure the offset of observed flux from that template flux in each filter. For normally distributed errors in flux measurements, the average of these offsets should be zero. However, we find systematic flux offsets between the observed flux and the template flux for each filter. We wish to correct the filters zero point by the median offset in each filter. For this calculation we restrict our sample to sources with spectroscopic redshifts and high-S/N detections, in this case expected SED template fluxes of at least five times the detection limit for the filter. We calculate the median flux offset for each filter, iterating by applying the calculated flux offsets and refitting the SEDs. Within three iterations, these flux offsets vary by less than 1%, and we find that slightly altering the list of sources used to calculate these flux offsets does not affect our solutions by more than 1%–2%. Therefore our photometry is systematically uncertain at this level. For each band, we apply these photometric offsets, listed in Table 6, before computing final photometric redshifts used in this paper. We do not calculate offsets for the IRAC bands where the templates have greater uncertainties.

6.4. Flux Comparison to other Catalogs

The region around the MUSYC-ECDF-S has been observed by many surveys and therefore there are many public catalogs available in this region. We refer to Taylor et al. (2009) for a detailed list of these surveys and a quantitative comparison of their photometry. Here we briefly compare our catalog to two previous versions of the MUSYC catalog, from Gawiser et al. (2006b) and Taylor et al. (2009), and to the updated photometry

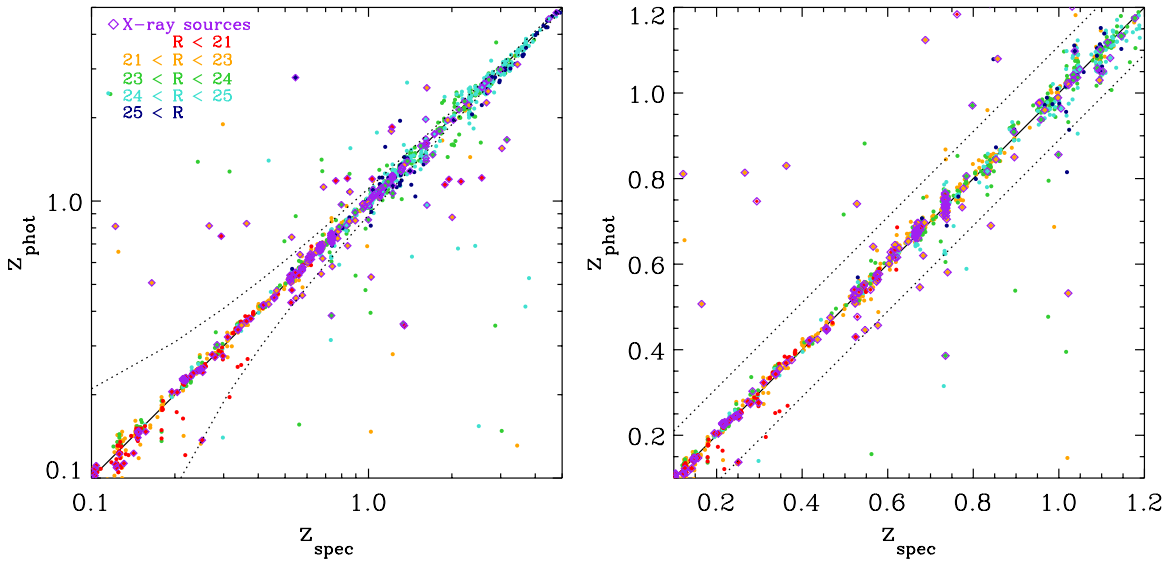

Figure 8. Left: comparison of photometric and spectroscopic redshifts for all high-quality spectroscopic redshifts (Table 5) and photometric redshift fits with $Q_z \leqslant 1$. The galaxies are colored by the *R*-band magnitude, and those detected in X-rays are also indicated by purple diamonds. We find $\Delta z/(1+z) \sim 0.008$, or $\Delta z/(1+z) \sim 0.006$ at $0.1 \leqslant z \leqslant 1.2$, where the Balmer break falls into the wavelength range covered by our medium-band filters. Dotted lines are set at 10 × NMAD, our definition of outliers. Right zoom-in on the low-redshift region with linear scale.

(A color version of this figure is available in the online journal.)

Table 7
Photometric Redshift Quality Versus Source Magnitude

Magnitude	No. of Objects	$Q_z \leqslant 1$	$l68_z - u68_z$	No. of $z_{\rm spec}$	$\Delta z/(1+z)$	σ_z	Outliers
$17 < R < 19$	283	99%	0.011	20	0.004	0.005	5%
$19 < R < 20$	385	98%	0.012	32	0.005	0.006	3%
$20 < R < 21$	733	98%	0.014	81	0.006	0.008	1%
$21 < R < 22$	1676	97%	0.015	167	0.006	0.007	2%
$22 < R < 23$	3537	93%	0.017	374	0.006	0.008	2%
$23 < R < 24$	8087	86%	0.022	524	0.007	0.011	6%
$24 < R < 25$	17048	68%	0.038	415	0.014	0.020	5%
$25 < R < 26$	25628	31%	0.063	77	0.019	0.032	6%
$26 < R$	26127	6%	0.121	7	0.021	0.026	14%
X-ray sources	825	69%	0.022	236	0.008	0.012	12%

of the Combo-17 medium-band catalog (Wolf et al. 2008). Each of these catalogs used slightly different techniques to derive the PSF-matched photometry, but all used SExtractor for detection and the same publicly available data. On average our fluxes are within 1% of those quoted by Gawiser et al. (2006b). For the comparison to Taylor et al. (2009) and Wolf et al. (2008), we include the offsets calculated in Section 6.3. Our photometry agrees with that published by Taylor et al. (2009) on average to ~ 0.02 mag, and with that of Combo-17 (Wolf et al. 2008) with an offset of -0.05 mag.

6.5. Photometric Redshifts

Comparing non-X-ray sources with high-quality spectroscopic redshifts, we find a median accuracy $\Delta z/(1+z) \sim 0.008$[22] out to $z \sim 5$ (Figure 8, left). Limiting ourselves to the subsample of sources with photometric redshifts $0.1 \leqslant z \leqslant 1.2$, where the Balmer break falls within our medium bands, we find $\Delta z/(1+z) \sim 0.006$ (Figure 8, right). We report the NMAD[23] for comparison with the works of others (e.g., Ilbert et al. 2006; Brammer et al. 2008; Taylor et al. 2009), and refer to it with the symbol $\sigma_z \sim 0.01$. We define outliers as $10 \times \sigma_z$, and find that ∼5% of the overall sample are labeled as outliers.

In Table 7, we show the photometric redshift quality as a function of galaxy magnitude; listing the magnitude bin, number of objects found within the given magnitude bin, the percent of the galaxies in the bin with $Q_z \leqslant 1$, the median 68% confidence interval for the galaxies in the bin as determined by EAzY, the number of galaxies in the bin with high-quality spectroscopic redshifts, the median $\Delta z/(1+z)$, σ_z and the percent of galaxies in the bin with spectroscopically confirmed redshifts that are outliers. The number of high-quality comparison spectroscopic redshifts is a strong function of magnitude, but

[22] $\Delta z = |z_{\rm spec} - z_{\rm phot}|$.

[23] We calculate the normalized median absolute deviation (NMAD) as

$$\sigma_{\rm NMAD} = 1.48 \times \text{median}\left|\frac{\Delta z - \text{median}(\Delta z)}{1+z_{\rm spec}}\right|$$

as in (Brammer et al. 2008). The normalization factor of 1.48 ensures that the NMAD of a Gaussian distribution is equal to its standard deviation and the subtraction of median (Δz) corrects any offset from zero of the Gaussian. The NMAD is a useful measure of dispersion because it is less sensitive to outliers than the standard deviation (Ilbert et al. 2006; Brammer et al. 2008).

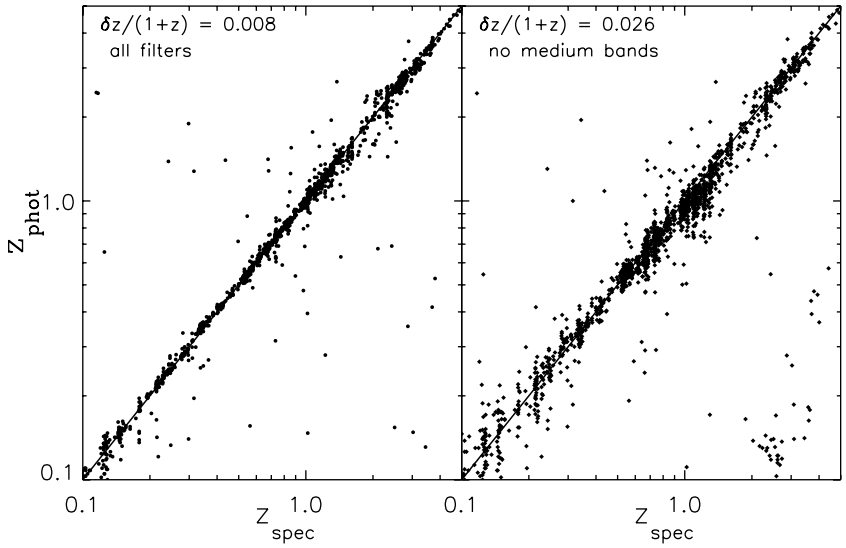

Figure 9. Comparison of photometric redshift vs. z_spec for all sources with high-quality spectroscopic redshifts and photometric redshift fits with $Q_z \leqslant 1$. Note that the left panel, which includes the additional medium-band filters in the fit, lowers the overall dispersion between the spectroscopic and photometric redshifts.

Table 8
Photometric Redshift Accuracy Versus Redshift

$z_{\rm phot}$	No. of $Q_z \leqslant 1$	$l68_z - u68_z$	$Q_z \leqslant 1$ (% of $z_{\rm spec}$)	No. of $z_{\rm spec}$	$\Delta z/(1+z)$	σ_z	outliers
$0 < z$	31381	0.034	92%	1697	0.008	0.011	4%
$0 < z < 1.2$	22318	0.024	98%	1242	0.006	0.008	3%
$1.2 < z < 3.7$	8547	0.087	80%	433	0.019	0.027	8%
$3.7 < z$	516	0.065	92%	21	0.012	0.016	5%

overall we maintain median $\Delta z/(1+z) \lesssim 0.01$ ($\sigma_z \lesssim 0.02$) to an R-band magnitude of 25. The scatter in the photometric versus spectroscopic redshifts almost certainly underestimates the actual uncertainty in the redshifts (Brammer et al. 2008), and therefore we use the median 68% confidence intervals computed by EAzY to compare the quality of the photometric redshifts for all galaxies. This confidence interval is the difference between the 68% confidence upper and lower bounds on the photometric redshift computed from the probability distribution $p(z)$ (Brammer et al. 2008) and is a strong function of galaxy apparent magnitude. We find good quality photometric redshifts ($Q_z \leqslant 1$; Brammer et al. 2008) down to the R-band magnitude of 25 for 70% of the sample (90% of the sample has $Q_z \leqslant 3$), but miss a large fraction of the galaxy population at fainter magnitudes. For many of the remaining sources poor fits are obtained by EAzY because the photometry is too uncertain, due to faintness of the sources, or intrinsic variability in the source over the time period of which the photometry was taken (Salvato et al. 2009). There are also cases where the intrinsic SED may not be matched by the templates and/or degeneracies in color-z space result in multiple peaks in the redshift–probability distribution. We note that when considering X-ray counterparts (Figure 8, purple diamonds), our accuracy is maintained $\Delta z/(1+z) \sim 0.009$, but the outlier fraction increases to 18%. We include the X-ray counterparts in the last line of Table 7 for comparison.

Additionally, we compare the photometric redshift accuracy as a function of redshift in Table 8. Because the spectroscopic sample contains a variety of selection effects (Section 6.2), Table 8 includes the median 68% confidence intervals computed by EAzY for all objects with $Q_z \leqslant 1$. We use photometric redshift to select the sources in each redshift bin so that we are comparing comparable sources in our measurements of $l68_z - u68_z$ and σ_z. Comparing to the galaxies with spectroscopically determined redshifts, the completeness of the photometric redshift determinations ($Q_z \leqslant 1$) varies as a function of redshift. We fit high-quality photometric redshifts to over 90% of galaxies, but we note that the completeness falls to 80% in the interval between $1.2 < z < 3.7$. Overall, with medium-band photometry we have achieved highly accurate photometric redshifts for the majority of the sources in the ECDF-S. The photometric redshifts are available online through the MUSYC Web site.[24]

We quantify the effect of the medium-band filters, comparing the photometric redshifts with and without the additional information these filters provide. When excluding the medium-band filters, we retain the broadband optical filters, as well as the J, H, K band and IRAC photometry. Overall, the medium-band filters provide a factor of 3 improvement over photometric redshifts using broadband filters alone, decreasing the median $\Delta z/(1+z)$ from 0.026 to 0.008 (comparing sources with $Q_z \leqslant 1$). We note that with the addition of the medium-band filters, high-quality($Q_z \leqslant 1$) photometric redshifts are obtained for 20% more of the spectroscopic redshift sample. The improvement is most noticeable at $0.1 \leqslant z \leqslant 1.2$ where the median$|\Delta z/(1+z)|$ falls from 0.022 to 0.006 and at $z \geqslant 3.7$ where the median $\Delta z/(1+z)$ falls from 0.024 to 0.006. These redshift intervals are where the Balmer break (3700 Å) and Lyman limit (912 Å) fall inside the region of the spectrum covered by the medium-band filters. However, we still see improvement at $1.2 \leqslant z \leqslant 3.7$, where the median $\Delta z/(1+z)$ falls from 0.032 to 0.016. In Figure 9, we compare the spectroscopic sources with good fits to the SEDs ($Q_z \leqslant 1$) with (left) and without (right) the

[24] http://physics.rutgers.edu/~gawiser/MUSYC

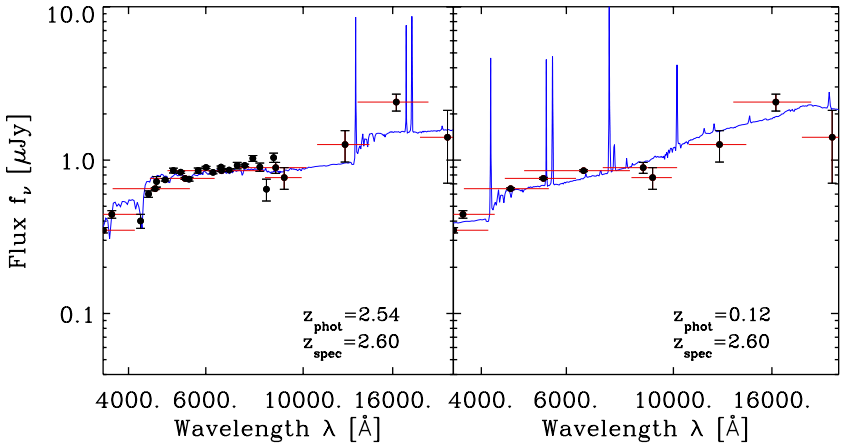

Figure 10. Example source at $z \sim 2.5$ and $R_{\rm AB} \sim 24$, red lines indicate the FWHM of the broadband filters. Here the medium-band photometry increases the photometric redshift, ruling out the erroneous low-redshift solution found by fitting the SED with only broadband photometry. In the case of the broadband photometry alone, a Balmer break is fit to the *UBV* bands; when the medium-band photometry is added, this same region is found to fit the sharper Lyα decrement instead.

(A color version of this figure is available in the online journal.)

medium-band filters. The medium-band filters not only tighten the accuracy around the z_phot $= z$_spec line, but also can help to rule out false redshift solutions (so called catastrophic failures) for sources with z_spec $\geqslant 1.2$. In each of these cases at $2 \sim 2.5$, the broadband photometry alone is fit with by a Balmer break feature in the SED at low redshift ($z \sim 0.1$) but when the medium-band photometry is added, the same optical region of the SED is fit by an Lyα decrement caused by absorption by the intergalactic medium (IGM) and the photometric redshift increases to a value more consistent with the spectroscopic determination. An example is shown in Figure 10, for a source with $R_{\rm AB} \sim 24$ and $z_{\rm spec} \sim 2.5$.

6.6. Star/Galaxy Separation

We use two methods to identify the stars in our catalog, the first using a $Bz'K$ color selection (Taylor et al. 2009) and the second fitting stellar SED templates (Ilbert et al. 2009).

The $Bz'K$ diagram is traditionally used to select moderate redshift ($z \gtrsim 1.4$) galaxies (Daddi et al. 2004), but is also an efficient discriminating between stars and galaxies (e.g., Daddi et al. 2004; Blanc et al. 2008; Taylor et al. 2009). Because our filter set is slightly different from that used by Daddi et al. (2004), we apply the offsets determined by Blanc et al. (2008) of -0.04 mag in $(z - K)$ and 0.56 mag in $(B - z)$ to our colors before plotting them in the BzK diagram. In Figure 11, we show the BzK diagram for at all sources in our catalog with $K_{\rm AB} \leqslant 21.84$ (i.e., $K_{\rm vega} \leqslant 20$). The stellar sequence is clearly separated from the galaxies by the colors $z-K \leqslant 0.3(B-z)-0.5$, shown as a solid black line in Figure 11. For comparison, we include the handful of spectroscopically identified stars (large blue + in Figure 11). Only 2 of the 108 spectroscopically identified ($K_{\rm AB} \leqslant 21.84$) stars are missed by the BzK star color selection. Although this method of color selection is effective at identifying stars, we are limited to the sources bright enough to be detected in our relatively shallower K-band coverage.

To identify stars in all of our objects with photometric redshifts, we evaluate a χ^2 value for $z = 0$ stellar SED template (Pickles 1998) fits for each object. Since the Pickles (1998) templates do not go past 2.5 μm, we do not include the *Spitzer* IRAC bands in the stellar fits. We flag as potential stars objects with reduced $\chi^2_{\rm star} \geqslant \chi^2_{\rm galaxy}$. These sources are

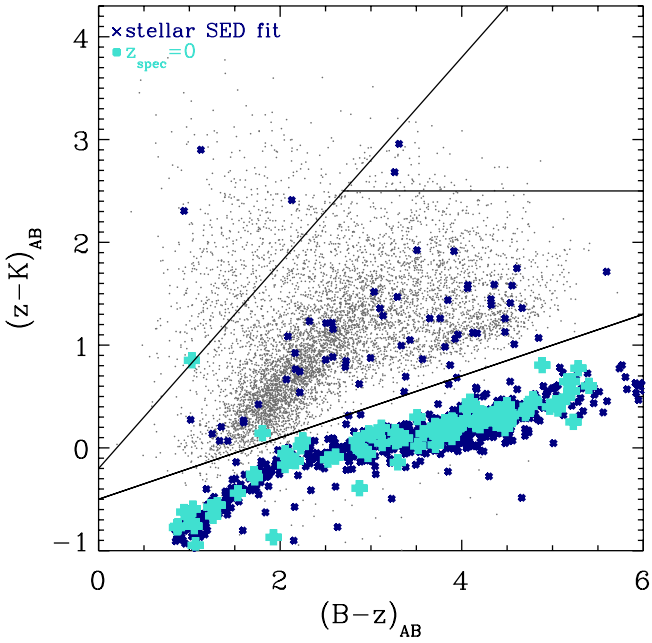

Figure 11. *Bzk* color–color diagram indicating stars. Note in this figure the $z - K$ magnitude has been adjusted by -0.04 and the $B - z$ magnitude by +0.56 to match the filter set used by Daddi et al. (2004). Sources with spectroscopic redshifts $z = 0$ (turquoise +) and those which fit stellar SEDs (dark blue ×), mostly lie along the stellar sequence in the bottom region. Also indicated are high-redshift BzK galaxies including star-forming *sBzK* galaxies (top left) and passive *pBzK* galaxies (top right). Overall, stars selected by template fitting to stellar SEDs are consistent with those indicated here on the BzK diagram.

(A color version of this figure is available in the online journal.)

included in the BzK diagram as blue crosses. The stars identified through template fitting agrees well with those selected in our BzK color selection, ~90% of stellar-template stars with $K_{\rm AB} \leqslant 21.84$ have BzK colors of stars (Figure 11, dark blue crosses). Additionally, 80% of BzK-color-selected stars are also identified as stars by the stellar template fit. Finally, we look at the subset of sources detected in the GEMS imaging (Häussler et al. 2007). Selecting sources with stellar FWHM from the GEMS imaging, ~80% of them are selected by our template-fitting method as stars, similar to the 84% of point-like sources that the COSMOS team identifies as stars through SED fitting (Ilbert et al. 2009). Furthermore, looking at bright ($R \lesssim 24$)

extended sources in the GEMS imaging, we find fewer than 2% are misidentified as stars by this template fit classification.

6.7. Comparison to Combo-17 Photometric Redshifts

Combo-17 produced the first highly accurate photometric redshifts of the ECDF-S region, and we wish to compare our own photometric redshifts to theirs (Wolf et al. 2004). We restrict ourselves to the brighter photometry ($r \leqslant 24$) where their published photometric redshifts are more reliable (10% accuracy), restricting ourselves to $r \leqslant 22$, we have fewer sources for comparison, but the accuracy of Combo-17 (2%) approaches our own (Wolf et al. 2004). To examine our consistency, we compare our photometric redshifts to those determined in Combo-17 for all sources contained in both catalogs, finding $\Delta z/(1+z) \sim 0.011$ at $R \leqslant 22$ and $\Delta z/(1+z) \sim 0.029$ at $R \leqslant 24$. Therefore, our photometric redshift determinations are consistent with those determined by Combo-17 to within their errors.

To compare our respective accuracies, we use spectroscopic sources (Figure 12), and compare z_spec with photometric redshifts for Combo-17 and our MUSYC Survey. For $R \leqslant 22$, we find $\Delta z/(1+z) \sim 0.011$ for Combo-17 and $\Delta z/(1+z) \sim 0.005$ for MUSYC, and considering all sources $R_{\rm AB} \leqslant 24$ we find $\Delta z/(1+z) \sim 0.025$ for Combo-17 and $\Delta z/(1+z) \sim 0.007$ for our MUSYC redshifts. Therefore we find that although our photometric redshifts agree with those from Combo-17 survey to within their respective uncertainties, the larger number of deeper medium-band filter observations in the MUSYC Survey improves the photometric redshift accuracy and extend this accuracy to fainter source populations. We note that these differences come not only from the deeper medium-band data, but also by including *JHK* and IRAC photometry.

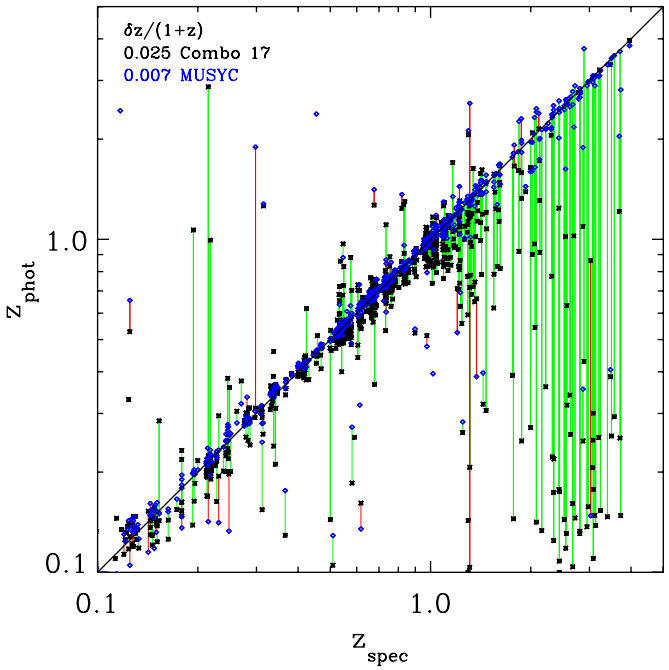

Figure 12. Comparison of our photometric redshifts (blue diamonds) to those of Combo-17 (black X). Where our photometric redshift is closer to that determined from spectroscopy than that from Combo-17, a green line connects the two photometric redshift determinations. Where the photometric redshift from Combo17 is closer to that determined from spectroscopy, a red line connects the two photometric redshift determinations. Overall, our photometric redshifts $\Delta z/(1+z)$ are more accurate for many sources that were outliers in Combo-17.

(A color version of this figure is available in the online journal.)

7. THE RED SEQUENCE TO $z \sim 1$

Here we demonstrate the quality of our data by showing the color–magnitude relation as a function of redshift in the E-CDFS. The colors and morphologies of galaxies form a bimodal population (Blanton et al. 2003; Baldry et al. 2004). This bimodality represents a fundamental relationship between mass and star formation history in galaxies, because the color of a galaxy is a proxy for the stellar age, where blue galaxies are younger and red galaxies are older. The red sequence contains the brightest galaxies, which typically have early-type morphologies, while the blue cloud galaxies typically have late-type morphologies. Relatively few galaxies are observed in the green valley, suggesting that galaxies spend only a short time here. *How* the bimodal galaxy population was created is one of the outstanding questions in galaxy studies today.

Rest-frame fluxes were computed following the procedure of Brammer et al. (2009), which measures the rest-frame fluxes from the best-fitting template (Wolf et al. 2003). This procedure is very different from a *K*-correction as it uses the observed medium bands that are closest in observed wavelength to the redshifted rest-frame band of interest. The Brammer et al. (2009) methodology is embedded in the EAzY photometric redshift code (Brammer et al. 2008).

In Figure 13, we show the distribution of galaxies in the rest-frame $U-V$ versus V plane. This plot most directly relates observables to the bi-modal color sequence as a function of redshift. The rest-frame $U-V$ color covers the Balmer break and therefore is a good measure of recent star formation and the luminosity in the V band is a proxy for stellar mass. In Figure 13, we also include the red sequence cut defined by Bell et al. (2004) in the Combo-17 survey (green dashed line) and our completeness limits in each redshift bin (blue solid line). We see a sequence of red points separated from the main blue clump of galaxies at all redshifts in our sample, highlighting the quality of our data. The location of this red sequence is consistent with that found by Bell et al. (2004).

7.1. Passive Galaxy Evolution

In color space both passive galaxies and dusty galaxies can appear red in $U-V$ colors. To investigate the nature of the red sequence (Figure 13), we use the IRAC photometry to separate out red passively evolving galaxies from red, dusty, star-forming galaxies. The rest-frame $V-J$ color can distinguish between these two populations because dust-free galaxies are blue in $V-J$ color, while the dust-obscured galaxies are still red (Labbé et al. 2005; Wuyts et al. 2007). Following Williams et al. (2009), we use a color–color diagram, rest-frame $U-V$ versus $V-J$, to investigate the nature of the bimodal galaxy color sequence for all galaxies with $0.2 \leqslant z \leqslant 1.2$ (Figure 14). We color code the galaxies from the red sequence on the color–magnitude diagram red using Bell et al.'s (2004) red sequence cut. As expected, we find that passive and star-forming galaxies separate cleanly in color–color space (see Williams et al. 2009).

We find that just over 20% of the galaxies identified as red sequence members in Figure 13 have rest-frame $V-J$ colors which place them in the star-forming sequence, consistent with previous work at these redshifts using morphological information (e.g., Ruhland et al. 2009) and with the results in Brammer et al. (2009) and K. E. Whitaker et al. (2010, in

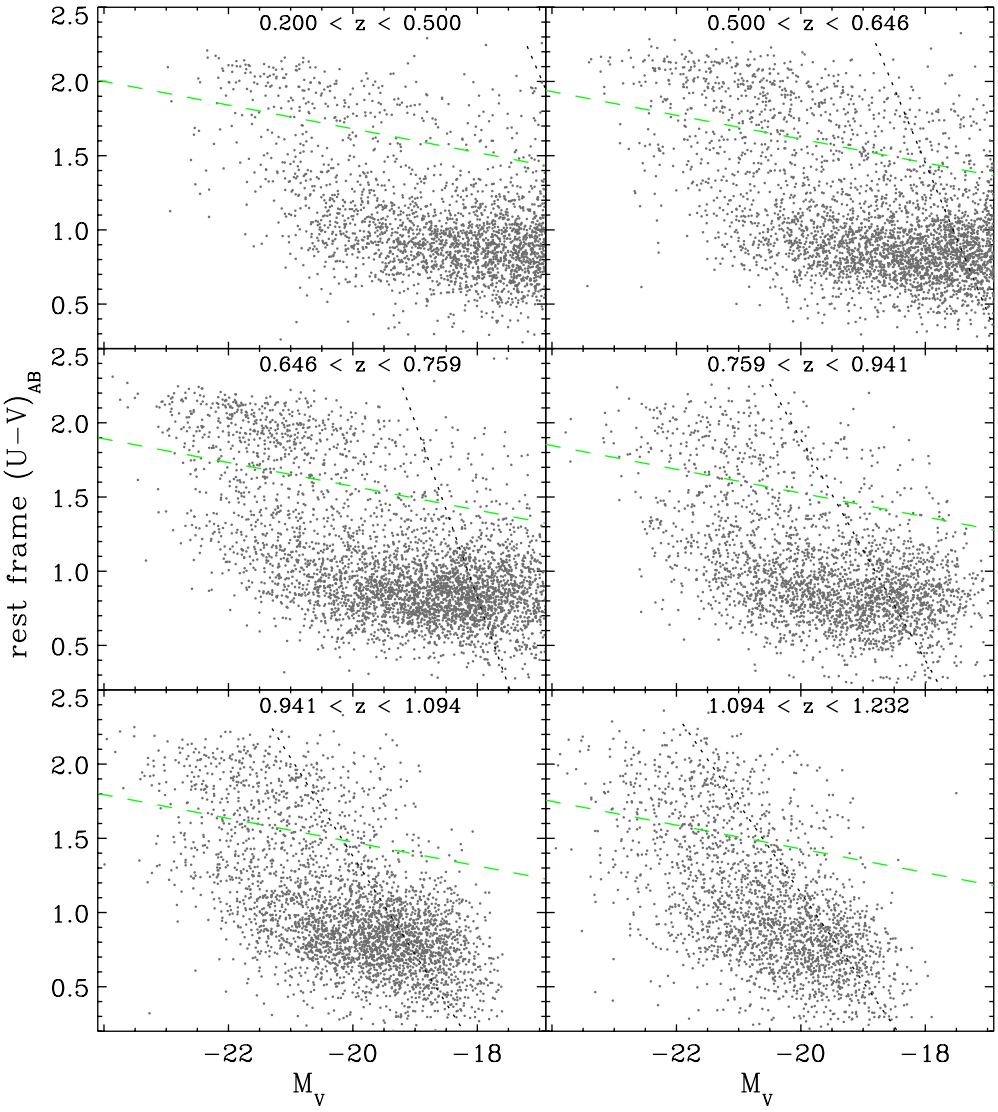

Figure 13. Rest-frame color–magnitude diagrams for galaxies as a function of redshift. The redshift bins represent equal steps of comoving volume, doubled in the last three bins. The green line is the red sequence cut defined by Bell et al. (2004) and the dotted line shows the 90% completeness limit. The red sequence is clearly present out to $z \sim 1.2$, where our redshift accuracy begins to fall. The red sequence contains the most luminous galaxies, while the blue cloud dominates the overall number density, especially for the fainter galaxies.

(A color version of this figure is available in the online journal.)

preparation). Splitting our redshift interval in two ($0.4 < z < 0.9$ and $0.9 < z < 1.2$) the fraction of red sequence galaxies with dusty colors is consistent between the two bins (21% and 23%, respectively).

8. SUMMARY

In this paper, we present new deep 18-medium-band photometry in the well-studied E-CDFS field. We reduced the raw data for the medium-band Subaru Suprime-Cam observations using a combination of standard routines and custom tasks. The (public) catalog includes photometry from 10 ground-based broadband images (U, $U38$, B, V, R, I, z, J, H, K), 4 IRAC images (3.6 μm, 4.5 μm, 5.8 μm, 8.0 μm), and 18 medium-band images ($IA427$, $IA445$, $IA464$, $IA484$, $IA505$, $IA527$, $IA550$, $IA574$, $IA598$, $IA624$, $IA651$, $IA679$, $IA709$, $IA738$, $IA767$, $IA797$, $IA856$). The full catalog provides multiwavelength SEDs for ~80,000 galaxies in the ECDF-S down to $R_{[AB]} \sim 27$ (40,000 at $R \leqslant 25.2$, the median depth of the medium-band imaging), although the accuracy and completeness of the photometric redshifts declines at $R \gtrsim 25.5$.

We computed accurate photometric redshifts using EaZy, a public photometric redshift code. The addition of the medium band proves a factor of 4 improvement in the photometric redshift accuracy over the use of broadband filters alone. Comparing to spectroscopic redshifts, we find a scatter in $\Delta z/(1+z)$ of 0.008 for the full sample, 0.006 at $0.2 < z < 1.2$ where the Balmer break is covered by the medium-band filters and 0.01 at $z \geqslant 3.7$ where the Lyman limit (912 Å) is covered by the medium-band filters. We find that the additional filters in the optical region even improve the photometric redshifts for sources at $1.2 \geqslant z \geqslant 3.7$, decreasing the median $\Delta z/(1+z)$ from 0.03 to 0.02.

We demonstrate that these photometric redshifts are sufficiently accurate to determine precise rest-frame colors of the galaxies. We detect the bimodal galaxy distribution out to $z \sim 1.2$ and find that 20% of the galaxies on the red sequence

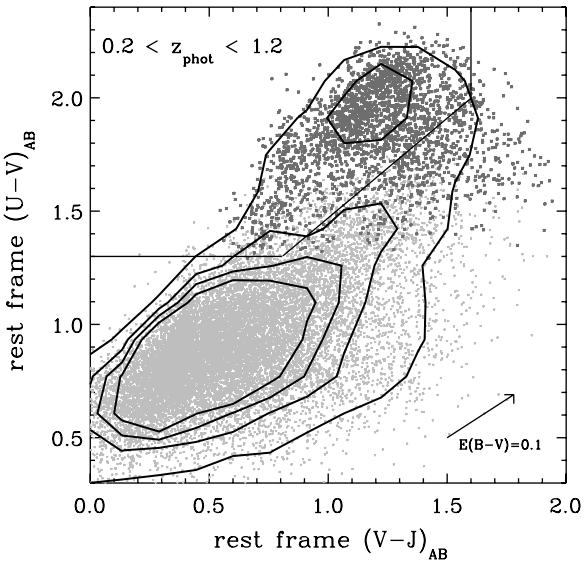

Figure 14. Rest-frame color–color diagram, showing $U-V$ vs. $V-J$ (Labbé et al. 2005; Williams et al. 2009). A bimodal color sequence is clearly visible separated by the dark lines (Williams et al. 2009). Dust-free quiescent galaxies are blue in $V-J$, therefore the peak of galaxies at red $U-V$ and bluer $V-J$ is passive red sequence galaxies. All galaxies with the Bell et al. (2004) red sequence cut are shown as darker points. This diagram identifies 20% of those red sequence galaxies as dusty star-forming galaxies rather than containing passive older stellar populations.

have longer wavelength colors consistent with being dusty. In keeping with the spirit of the MUSYC collaboration, we provide public access to the images, photometry, and photometric redshifts. In future papers, we will combine these accurate redshifts with the extensive ancillary data in the ECDF-S.

We thank the referee for helpful comments which improved this paper. Support from NSF grants AST-0407295, AST-0449678, AST-0807570, NASA JPL grants 1277255 and 1282692, and Yale University is gratefully acknowledged. Support for the work of K.S. was provided by NASA through Einstein Postdoctoral Fellowship grant number PF9-00069 issued by the Chandra X-ray Observatory Center, which is operated by the Smithsonian Astrophysical Observatory for and on behalf of NASA under contract NAS8-03060. We also thank Shunju Sasaki for help with the imaging and data reductions.

REFERENCES

Arnouts, S., et al. 2001, A&A, 379, 740
Baldry, I. K., Glazebrook, K., Brinkmann, J., Ivezić, Ž., Lupton, R. H., Nichol, R. C., & Szalay, A. S. 2004, ApJ, 600, 681
Balestra, I., et al. 2010, A&A, 512, A12
Bell, E. F., et al. 2004, ApJ, 608, 752
Benítez, N. 1999, in ASP Conf. Ser. 191, Photometric Redshifts and the Detection of High Redshift Galaxies, ed. R. Weymann et al. (San Francisco, CA: ASP), 31
Bertin, E., & Arnouts, S. 1996, A&AS, 117, 393
Blanc, G. A., et al. 2008, ApJ, 681, 1099
Blanton, M. R., et al. 2003, ApJ, 594, 186
Bolzonella, M., Miralles, J.-M., & Pelló, R. 2000, A&A, 363, 476
Brammer, G. B., van Dokkum, P. G., & Coppi, P. 2008, ApJ, 686, 1503
Brammer, G. B., et al. 2009, ApJ, 706, L173
Capak, P., et al. 2007, ApJS, 172, 99
Cardamone, C. N., et al. 2008, ApJ, 680, 130
Cardelli, J. A., Clayton, G. C., & Mathis, J. S. 1989, ApJ, 345, 245
Cimatti, A., et al. 2002, A&A, 392, 395
Cristiani, S., et al. 2000, A&A, 359, 489
Croom, S. M., Warren, S. J., & Glazebrook, K. 2001, MNRAS, 328, 150
Daddi, E., Cimatti, A., Renzini, A., Fontana, A., Mignoli, M., Pozzetti, L., Tozzi, P., & Zamorani, G. 2004, ApJ, 617, 746
Damen, M., et al. 2010, submitted
Davis, M., et al. 2003, Proc. SPIE, 4834, 161
Fazio, G. G., et al. 2004, ApJS, 154, 10
Franx, M., et al. 2003, ApJ, 587, L79
Gawiser, E., et al. 2006a, ApJ, 642, L13
Gawiser, E., et al. 2006b, ApJS, 162, 1
Grazian, A., et al. 2006, A&A, 449, 951
Häussler, B., et al. 2007, ApJS, 172, 615
Hildebrandt, H., et al. 2006, A&A, 452, 1121
Ilbert, O., et al. 2006, A&A, 457, 841
Ilbert, O., et al. 2009, ApJ, 690, 1236
Iye, M., et al. 2004, PASJ, 56, 381
Kennicutt, R. C., Jr. 1998, ARA&A, 36, 189
Kriek, M., et al. 2008, ApJ, 677, 219
Krisciunas, K., et al. 1987, PASP, 99, 887
Kron, R. G. 1980, ApJS, 43, 305
Labbé, I., et al. 2003, AJ, 125, 1107
Labbé, I., et al. 2005, ApJ, 624, L81
Le Fèvre, O., et al. 2004, A&A, 428, 1043
Le Fèvre, O., et al. 2005, A&A, 439, 845
Miyazaki, S., et al. 2002, PASJ, 54, 833
Moy, E., Barmby, P., Rigopoulou, D., Huang, J.-S., Willner, S. P., & Fazio, G. G. 2003, A&A, 403, 493
Muller, G. P., Reed, R., Armandroff, T., Boroson, T. A., & Jacoby, G. H. 1998, Proc. SPIE, 3355, 577
O'Donnell, J. E. 1994, ApJ, 422, 158
Ouchi, M., et al. 2004, ApJ, 611, 685
Pickles, A. J. 1998, PASP, 110, 863
Quadri, R., et al. 2007, AJ, 134, 1103
Richards, G. T., et al. 2006, ApJS, 166, 470
Rieke, G. H., et al. 2004, Proc. SPIE, 5487, 50
Ruhland, C., Bell, E. F., Häußler, B., Taylor, E. N., Barden, M., & McIntosh, D. H. 2009, ApJ, 695, 1058
Salvato, M., et al. 2009, ApJ, 690, 1250
Schlegel, D. J., Finkbeiner, D. P., & Davis, M. 1998, ApJ, 500, 525
Strolger, L.-G., et al. 2004, ApJ, 613, 200
Szokoly, G. P., et al. 2004, ApJS, 155, 271
Taniguchi, Y. 2004, in Studies of Galaxies in the Young Universe with New Generation Telescope, ed. N. Arimoto & W. J. Duschl (Sendai: JSPS-DFG), 107
Taylor, E. N., et al. 2009, ApJS, 183, 295
Treister, E., et al. 2009a, ApJ, 706, 535
Treister, E., et al. 2009b, ApJ, 693, 1713
Vanden Berk, D. E., et al. 2001, AJ, 122, 549
van der Wel, A., Franx, M., van Dokkum, P. G., & Rix, H.-W. 2004, ApJ, 601, L5
van Dokkum, P. G., et al. 2009, PASP, 121, 2
Vanzella, E., et al. 2008, A&A, 478, 83
Williams, R. J., Quadri, R. F., Franx, M., van Dokkum, P., & Labbé, I. 2009, ApJ, 691, 1879
Wolf, C., Hildebrandt, H., Taylor, E. N., & Meisenheimer, K. 2008, A&A, 492, 933
Wolf, C., Meisenheimer, K., Rix, H., Borch, A., Dye, S., & Kleinheinrich, M. 2003, A&A, 401, 73
Wolf, C., et al. 2004, A&A, 421, 913
Wuyts, S., Labbé, I., Schreiber, N. M. F., Franx, M., Rudnick, G., Brammer, G. B., & van Dokkum, P. G. 2008, ApJ, 682, 985
Wuyts, S., et al. 2007, ApJ, 655, 51
Yagi, M., Kashikawa, N., Sekiguchi, M., Doi, M., Yasuda, N., Shimasaku, K., & Okamura, S. 2002, AJ, 123, 66